Supplementary Information

An auxin-driven polarized transport model for phyllotaxis

Henrik Jönsson, Marcus Heisler, Bruce E. Shapiro, Elliot M. Meyerowitz and Eric Mjolsness

Contents

S1 Experimental details

S1.1 PIN1::GFP fusion construct

8763 bp of *Arabidopsis* genomic DNA were PCR amplified from IGF BAC F6D5 using the primers (5' CTGACAAGTGTCACGCCTCT3' and 5' CAAATCATGTGTCGACTTCCA3') and the amplified product was TA cloned into pGEMT easy (Promega). The mGFP5 (a gift from J. Hasseloff) coding regions was PCR-amplified with the primers (5' CTC GAG CAG TAA AGG AGA AGA ACT TTT CAC 3' and 5' CCT CGA GGC TTT GTA TAG TTC ATC CAT GCC 3') containing XhoI sites. This GFP clone was subsequently inserted in frame into a unique XhoI site located within the central hydrophilic region of the PIN1 protein. A NotI fragment containing the entire PIN1 genomic clone as well as GFP was then transformed into Ler plants in the pART27 binary transformation vector (1) using Agrobacterium-mediated transformation (2) and plants harboring the transgene were selected for kanamycin resistance. To test functionality, T1 transgenic lines were crossed to *pin1-4* heterozygotes. Five independent F3 families were identified that were homozygous for the *pin1-4* allele and segregating for the PIN1::GFP. In all lines complete rescue of the *pin1-4* phenotype co-segregated with the kanamycin resistance marker.

S1.2 Confocal microscopy

Tissue was prepared by applying 10 mg ml^{-1} FM4-64 (Molecular Probes) to intact inflorescences. After 30 minutes inflorescences were detached and fixed in 4% paraformaldehyde containing 0.1% Tween 20 and 0.1% Triton X-100 at 4° C for 1 hr. Mature buds were then dissected away and the meristem immersed in 50% glycerol under a coverslip ready for imaging using a Zeiss Plan-Apochromat 63x/1.40 NA objective. A 488 nm laser line was used to excite both GFP and FM4-64 and the emission was split using a 545 nm secondary dichroic.

S2 Computational and model details

S2.1 Template data extraction

The template extraction is performed in four steps from the confocal data [5]. (1) The background is extracted from the membrane image using a snake algorithm [12] initiated by manually clicking around the SAM. (2) Cell compartments are extracted in the membrane marked picture using a watershed type of algorithm [2]. As preprocessing, the image is smoothed using region averaging (intensity values are averaged using a region with a radius of ten pixels twice). The original resolution of the data is 0.15μm per pixel. This is followed by the use of a gradient descent algorithm on the intensity, starting from each individual pixel. All pixels ending up in the same intensity minimum are taken as

defining a cellular compartment. (3) Membrane/wall compartments are typically thinner than the pixel resolution of the data, so these compartments are created by defining pixel subsets within a cellular compartment that are immediate neighbors to another cellular compartment. The extracted compartments are shown in Figure 1B in the paper. (4) Using the pixel subsets extracted as compartments in the membrane image, the PIN1 image is used to extract average PIN1 intensities for each compartment (Figure 1C,D in the paper). These numbers are, for simplicity, interpreted as relative concentrations of PIN1.

S2.2 Detailed model on a cell-wall topology with experimental parameters

All reaction and transport mechanisms used in the model are provided in Table S1, and combined in Equations S1-S4. The compartmentalization and illustration of the transport/cycling are shown in Figure S1. Parameter values used are provided in Table S2. The compartmentalization is simplified to include a single cytoplasm compartment and surrounding each cytoplasm compartment are wall/membrane compartments toward each neighboring cell or the SAM boundary (Figure S1). The auxin model includes active and passive transport across membranes (between cellular and wall compartments), diffusion within the walls, and production and degradation. PIN1 is allowed to cycle between cellular and membrane compartments, but never moves between cells.

The model is a development of the models originally proposed by Goldsmith *et al* [1],

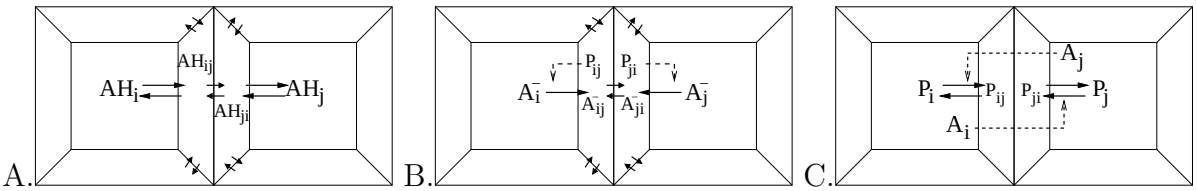

Figure S1: Illustration of the Auxin transport and PIN1 cycling models. A) AH (weak acid form) transport. B) A^- (anion form) transport. Note that also the A^- influx is dependent on P_{ij}. This rate is low compared to the efflux, and this mechanism is not illustrated in the figure. C) PIN1 cycling model.

and Mitchison [7]. We allow auxin to appear in two forms within the plant, a weak acid (AH) and anion (A^-) form. While AH can penetrate the membrane passively, A^- needs to be actively transported, which in our model is assumed to be mediated by PIN1 located at the membrane. We assume that the reaction $A^- + H \leftrightarrow AH$ is fast and the pH dependent equilibrium fractions are used. As the pH differs between cytoplasm and walls the fraction of the different auxin variants in different compartment types are explicitly accounted for ($f^{cell/wall}_{A^-/AH}$). These fractions are also dependent on $pK = -log(A^- H^+/AH)$, and are given by $f_{A^-} = 10^{pH-pK_d}/(1+10^{pH-pK_d})$, and $f_{AH} = 1/(1+10^{pH-pK_d})$. Since the PIN mediated active auxin transport is dependent on the electro-chemical gradient between the cytoplasm and the apoplast, additional asymmetric factors, $N_{efflux/influx}$, are used to describe the dependence on the membrane potential [1, 7, 6]. These factors are defined by $N_{influx} = N_{efflux}e^{\Phi} = \Phi e^{\Phi}/(e^{\Phi}-1)$, where $\Phi = zVF/RT$. z is the valence, V is the membrane potential, F is the Faraday constant, R is the gas constant, and T is the absolute temperature.

Cellular efflux is modeled using a passive transport rate defined as $D_{efflux} = p_{AH} f^{cell}_{AH}$, and an active rate defined by $T_{efflux} = p_{A^-} f^{cell}_{A^-} N_{efflux}$. The f^{cell}_{AH},$f^{cell}_{A^-}$ are the fractions

of the different auxin variants in the cell, p_{AH} and p_{A^-} are the membrane permeabilities, and N_{efflux} is the factor for efflux across the charged membrane. For influx from the walls to the cell, the passive and active rates are defined as $D_{influx} = p_{AH} f_{AH}^{wall}$ and $T_{influx} = p_{A^-} f_{A^-}^{wall} N_{influx}$, where the individual parameters are defined as previously. The resulting net auxin flux between a cellular compartment and its neighboring wall compartment is given in Equation 2 in the paper.

In addition to this, we allow for apoplastic auxin transport modeled as diffusion of both forms of auxin between neighboring wall compartments with a diffusion constant D_A. Also, in the final equations the volumes, distances and crossing areas of the compartments are accounted for.

It can be noted that since $f_{AH}^{wall} >> f_{AH}^{cell}$ passive transport results in higher influx to the cells compared to efflux. For the active transport term $N_{efflux} >> N_{influx}$ and the PIN1 mediated influx is negligible. Auxin is dependent on PIN1 for cellular efflux, while it passively crosses the membranes from the walls into the cells. While we simulate active auxin efflux, for simplicity active auxin influx is not explicitly defined in the model. We note that the phenotype of *aux1* mutants, impaired in auxin influx, is not as severe as the *pin1* phenotype. However, we also do simulations where passive influx is increased to approximate the activity of a homogeneous influx mediator.

Note that we use a single compartment for the cell cytosol, which means that we neglect spatial variations of auxin within the cell. For this to be a good approximation, the active

transport terms should be small compared to the internal diffusion. A crude estimation of this is to compare $D_A A/L$ with $p_{A^-} P_{membrane} f^{cell}_{A^-} N_{efflux} A$, where L is the cell length, $P_{membrane}$ is the PIN1 concentration in the membrane, A is the auxin concentration, and the other parameters are described above. This leads to values of about 140 and 50 respectively (using the maximal $P_{membrane} = 1\mu$moles per unit area, and $L = 5\mu$m). The diffusion term is larger, but since the difference is not too large it indicates that the model might be improved by including sub-compartments for the cytosol compartment.

The complete model is defined by the ODE equations

$$\begin{aligned}
\frac{dA_i}{dt} &= c_A - d_A A_i + \frac{1}{V_i}\left[p_{AH} \sum_{k\in\mathcal{N}_i} a_{ik} \left(f^{wall}_{AH} A_{ik} - f^{cell}_{AH} A_i \right) \right. && \text{(S1)} \\
&+ \left. p_{A^-} \sum_{k\in\mathcal{N}_i} a_{ik} P_{ik} \left(f^{wall}_{A^-} N_{influx} \frac{A_{ik}}{K_A + A_{ik}} - f^{cell}_{A^-} N_{efflux} \frac{A_i}{K_a + A_i} \right) \right], \\
\frac{dA_{ij}}{dt} &= -d_A A_{ij} + \frac{1}{V_{ij}} \left[a_{ij} \left\{ p_{AH} \left(f^{cell}_{AH} A_i - f^{wall}_{AH} A_{ij} \right) \right. \right. && \text{(S2)} \\
&+ \left. \left. p_{A^-} P_{ij} \left(f^{cell}_{A^-} N_{efflux} \frac{A_i}{K_a + A_i} - f^{wall}_{A^-} N_{influx} \frac{A_{ij}}{K_A + A_{ij}} \right) \right\} \right. \\
&+ \left. D_A \left\{ \frac{a_{ijij_l}}{d_{ijij_l}} \left(A_{ij_l} - A_{ij} \right) + \frac{a_{ijij_r}}{d_{ijij_r}} \left(A_{ij_r} - A_{ij} \right) + \frac{a_{ijji}}{d_{ijji}} \left(A_{ji} - A_{ij} \right) \right\} \right], \\
\frac{dP_i}{dt} &= \frac{1}{V_i} \sum_{k}^{N_i} a_{ik} \left(k_2 P_{ik} - P_i \frac{k_1 A_k^n}{K^n + A_k^n} \right), && \text{(S3)} \\
\frac{dP_{ij}}{dt} &= P_i \frac{k_1 A_j^n}{K^n + A_j^n} - k_2 P_{ij}. && \text{(S4)}
\end{aligned}$$

Cytoplasmic compartments are given by single indices (i, j, k) and wall/membrane compartments by double indices (ij, ik), and the summations are over the set of cellular neighbors $(\mathcal{N}_i)$ for a cytosol compartment i. The apoplastic diffusion terms in Eq. S2

Table S1: Model for molecular reactions and transport in the simulations on the template. Note that in some simulations the PIN1 extracted from the template is used and no PIN1 update is applied.

Row	Reaction/ Transport	Description	ODE contribution (rate/flux)	Parameters
1	$0 \rightarrow A_i$	Auxin production	c_A	c_A
2	$A_i \rightarrow 0$	Auxin degradation	$d_A A_i$	d_A
3	$A_{ij} \rightarrow 0$	Auxin degradation	$d_A A_{ij}$	d_A
4	$A_i \rightarrow A_{ij}$	Passive auxin (AH) transport, cell to wall	$a_{ij} D_{efflux} A_i$	$D_{efflux} = p_{AH} f_{AH}^{cell}$
5	$A_{ij} \rightarrow A_i$	Passive auxin (AH) transport, wall to cell	$a_{ij} D_{influx} A_{ij}$	$D_{influx} = p_{AH} f_{AH}^{wall}$
6	$A_{ij} \rightarrow A_{i'j'}$	Auxin diffusion within walls	$\frac{a_{iji'k}}{d_{iji'k}} D_A A_{ij}$	D_A
7	$A_i \overset{P_{ij}}{\rightarrow} A_{ij}$	Active PIN1 dep. auxin (A^-) transport, cell to wall	$a_{ij} T_{efflux} P_{ij} \frac{A_i}{K_A + A_i}$	$T_{efflux} = p_{A^-} f_{A^-}^{cell} N_{eff}$, K_A
8	$A_{ij} \overset{P_{ij}}{\rightarrow} A_i$	Active PIN1 dep. auxin (A^-) transport, wall to cell	$a_{ij} T_{influx} P_{ij} \frac{A_{ij}}{K_A + A_{ij}}$	$T_{influx} = p_{A^-} f_{A^-}^{wall} N_{inf}$, K_A
9	$P_i \overset{A_j}{\rightarrow} P_{ij}$	Auxin dependent PIN1 cycling, cell to membrane	$a_{ij} k_1 \frac{A_j^n}{K^n + A_j^n}$	k_1, K, n
10	$P_{ij} \rightarrow P_i$	Pin1 cycling, membrane to cell	$a_{ij} k_2 P_{ij}$	k_2

are explicitly given and each wall compartment has three neighbors, left and right neighbors connected to the same cell (ij_l, ij_r) and one neighbor "connected" to the neighboring cell (ji) cf. Figure S1 The auxin and PIN1 concentrations are given by A_a, P_a respectively. Spatial variables are taken from measurements in the experimental template and are constant during the simulations. These are compartmental volume, V_i and V_{ij}, crossing area between neighboring cytoplasm and membrane/wall compartments, a_{ij}, crossing areas between neighboring wall compartments, a_{ijji}, and distances between neighboring wall compartments as used in the diffusion term, d_{ijji}. Since the crossing area between neighboring wall compartments surrounding a cell is harder to extract from the template, we use a constant value of $a_{ijik} = 0.025\mu$m corresponding to a cell wall thickness of 50 nm. All parameters and values used in the simulations are presented in Table S2.

Table S2: Parameters used in the template simulations. Most of the parameters are taken from [1, 7, 6] and are further discussed in the text. In the ref column we only cite if exact the same value is used, but in most cases similar values are used.

Par	Definition	Value	Ref
pK	equilibrium constant for auxin variants	4.7	[1],[7]
pH^{cell}	pH in the cellular compartments	7.2	[1]
pH^{wall}	pH in wall compartments	5.0	[1],[7]
f_{AH}^{cell}	fraction AH/A in cells	0.003	[1]
f_{AH}^{wall}	fraction AH/A in walls	0.334	[1]
$f_{A^-}^{cell}$	fraction A^-/A in cells	0.997	[1]
$f_{A^-}^{wall}$	fraction A^-/A in walls	0.666	[1]
p_{AH}	membrane permeability AH	3.3×10^1 $\mu m s^{-1}$	[1]
p_{A^-}	membrane permeability A^-	1.24×10^1 $\mu m s^{-1}$	[1]
Vm	membrane potential	-100 mV	[1]
N_{influx}	Electrochemical factor for influx	0.07	[1]
N_{efflux}	Electrochemical factor for efflux	4.0	[1]
K_A	Half max Michaelis-Menten constant	1.0 μM	[7]
D_A	Auxin diffusion (in walls)	7×10^2 $\mu m^2 s^{-1}$	[1])
c_A	Auxin production / boundary influx	0.1 $\mu M s^{-1}$	
d_A	Auxin degradation / boundary effflux	0.1 s^{-1}	
k_1	Maximal PIN1 membrane localization rate	1.0 s^{-1}	optimized
k_2	PIN1 internalization rate	0.4 s^{-1}	optimized
n	Hill coefficient for PIN1 membranalization	3.0	optimized
K	Hill half max constant for PIN1 membranalization	0.4 μM	optimized

pK is from the equilibrium of the auxin variants The fractions of different auxin variants in different compartment types are pH dependent and the relation and values used are shown in Figure S2A. The N factors due to the membrane potential ($N_{influx} = N_{efflux}e^{\Phi} = \Phi e^{\Phi}/(e^{\Phi} - 1)$, where $\Phi = zVF/RT$) are calculated by using a membrane potential $Vm = -100mV$, a valence of 1, and using values for physical constants as follows. Faraday constant, $F = 9.6 \times 10^4$ As mol^{-1}, the gas constant, $R = 8.3$ Jmol^{-1}K^{-1}, and the absolute temperature, $T = 300$K. The dependence of these factors on the membrane potential is showed in Figure S2B. K_A is set within the region $K_A \in [0.3 : 2]\mu M$ as estimated by Mitchison [7]. The diffusion rate is from estimations of auxin diffusion in water. Simulations with a lower diffusion rate have been tried, and leads to similar re-

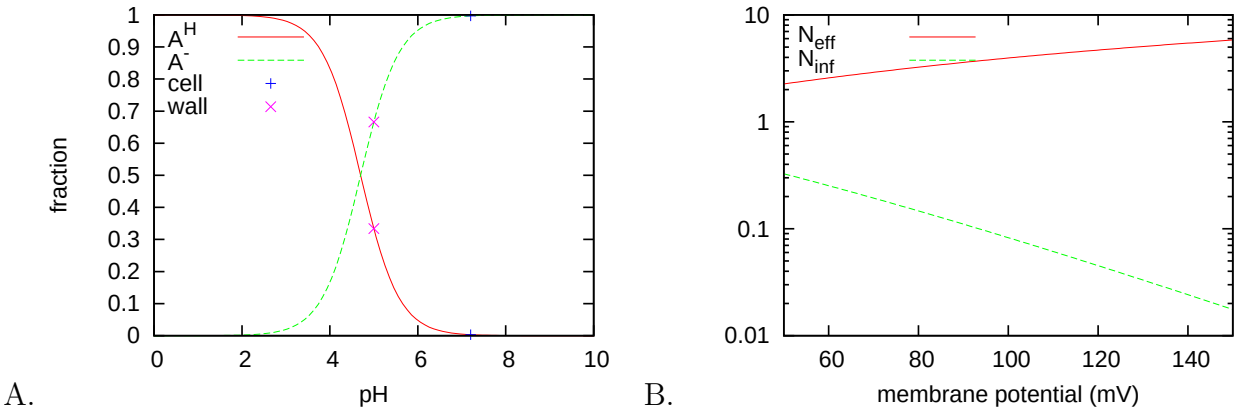

Figure S2: A) pH dependence of the fraction of the different auxin variants. The lines show the dependence and the points show the values used in the simulations. B) Membrane voltage dependence of the factors in the PIN1 mediated transport. The absolute value of the membrane potential is used on the x axis in the plot.

sults. Auxin is also allowed to be homogeneously produced and degraded in cells, where the auxin production term could also be interpreted as auxin transported into the simulated region from the cells outside of the region. There are no experimental estimates of these rates, and we have elaborated with different values, most leading to similar results as the presented ones (see e.g. Figure S5). It is an apparent problem to estimate the reliability and certainty of experimental parameter values. For example, other values for the membrane permeability constant of the protenated form of auxin appear in the literature [6]. This value is about a factor 60 times lower and might increase the need of an AUX mediated influx for our model. But introducing an influx mediator would also require knowledge of the positioning of the influx mediator and an estimate of its permeability constant which is currently unknown.

All simulations using a constant PIN1 distribution from the template, starts with a

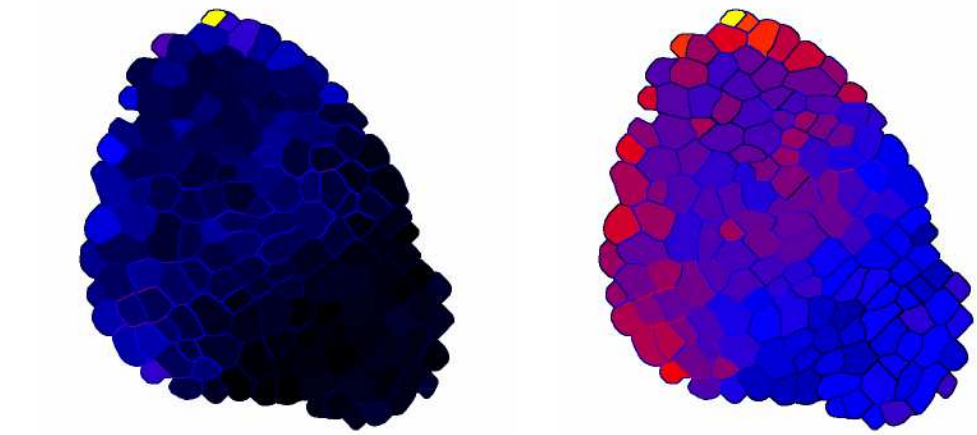

A. B.

Figure S3: Auxin equilibrium concentrations for simulations on the template with extracted PIN1 concentrations. K_A in the MM- description of active auxin concentration is varied from $K_A = 1$, to boundaries estimated in Mitchison [7]. A) $K_A = 0.3$. B) $K_A = 2.0$.

homogeneous auxin distribution (Figure 2 in the paper, and Figures S3-S5). In the simulation presented in Figure 4A in the paper, auxin is kept constant at the equilibrium from the constant PIN1 simulation (Figure 2A in the paper). Initial values for PIN1 are taken from the template, and the PIN1 cycling model is allowed to redistribute the PIN1 within each cell.

S2.2.1 Parameter sensitivity

To check the sensitivity to parameters, simulations where parameter values are changed one at a time are performed to see how the auxin distribution changes. In these simulations the PIN1 distribution is held constant. In Figure S3-S5 some examples are shown, and the conclusion from this analysis is that the qualitative behavior of the simulation is fairly robust.

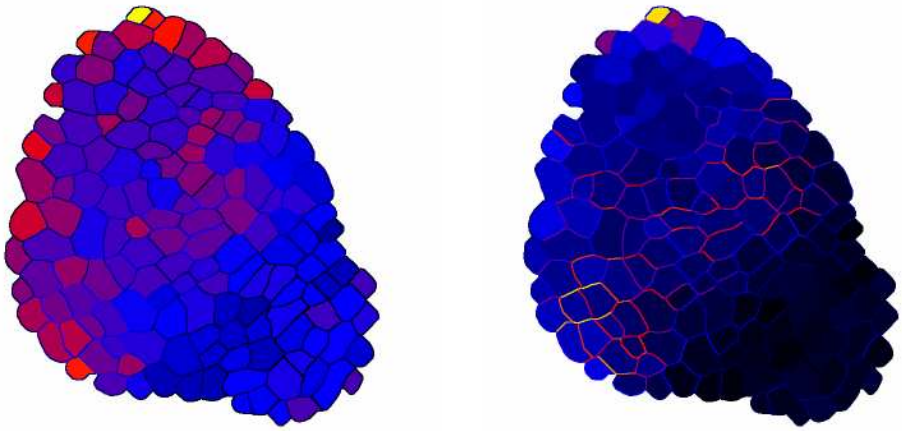

A. B.

Figure S4: Auxin equilibrium concentrations for simulations on the template with extracted PIN1 concentrations. The p_{A-} in the active auxin transport terms are varied twofold from the value $p_{A-} = 12.4$ estimated by Goldsmith [1]. A) $0.5p_{A-}$. B) $2.0p_{A-}$.

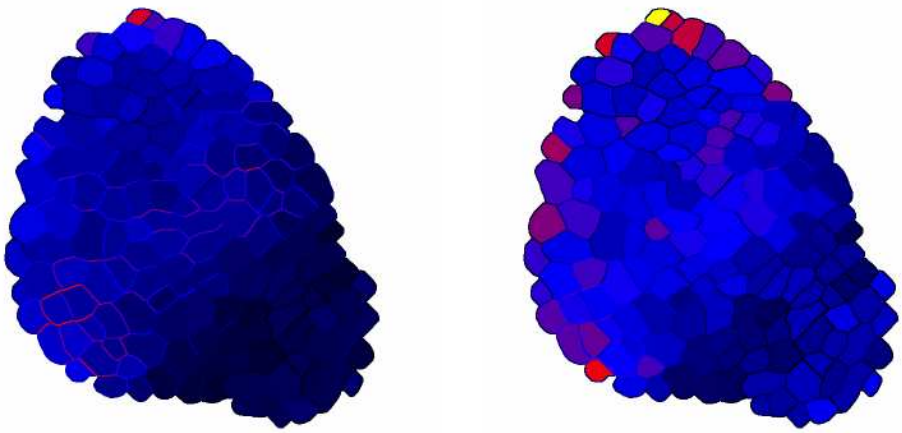

A. B.

Figure S5: Auxin equilibrium concentrations for simulations on the template with extracted PIN1 concentrations. The auxin levels (production) is varied twofold from the value $c_A = 0.1$. A) $0.5c_A$. B) $2.0c_A$.

Table S3: Model for molecular reactions and transport in the simulations including cellular growth and proliferation. X is only produced outside the apical region modeled using the step function $\Theta(x)$ which equals 1 for $x \geq 0$ and zero for $x < 0$.

Row	Reaction/ Transport	Description	ODE contribution (rate/flux)	Parameters
1	$0 \rightarrow A_i$	Auxin production	c_A	$c_A = 0.0$
2	$0 \rightarrow A_i$	Auxin prod. outside central zone.	$c_{A2} X_i$	$c_{A2} = 0.002$
3	$A_i \rightarrow 0$	Auxin degradation	$d_A A_i$	$d_A = 0.001$
4	$A_i \rightarrow A_j$	Passive auxin transport	$D A_i$	$D = 0.01$
5	$A_i \overset{P^*_{ij}}{\rightarrow} A_j$	Active PIN1 dep. auxin transport	$T P^*_{ij} \frac{A_i}{K_A + A_i}$	$T = 0.036$, $K_A = 1.0$
6	$0 \rightarrow X_i$	X production	$c_X \Theta(\sqrt{x_i^2 + y_i^2} - R_X)$	$c_X = 0.1, R_X = 1.5, 2.0$
7	$X_i \rightarrow 0$	X degradation	$-d_X X_i$	$d_X = 0.1$
8	$X_i \rightarrow X_j$	X diffusion	$D_X X_i$	$D_X = 0.01$

S2.3 Growth simulations using the cell-based model

For the simulations including cellular growth we use the cell-based model, where most spatial contributions are not accounted for in molecular reactions. Neither is the concentration decrease due to dilution in a growing cell accounted for. For simulating a simple shoot topology, cells are restricted to a half-sphere/cylinder surface with a radius $R = 7.0$ (Figure 5 in the paper). Cells are removed from the system when its position is below a threshold $z_{remove} = -15$ as measured from the half-sphere to cylinder connection at $z = 0$. In the reversal simulations, the cells are modeled on a two-dimensional plane (Figure 6 in the paper), and cells are removed outside a threshold radius $R_{th} = 13$. All reaction and transport mechanisms present in the model, together with parameter values used are presented in Table S3.

Auxin model

Equation 2 in the paper is used for describing the auxin transport, where i and j are two neighboring cells. As the model creates auxin peaks in cells that are moving out from the apical region, the apex would quickly be depleted from auxin unless new auxin is supplied. We have chosen to include homogeneous auxin input and output terms in the model to solve this problem. These terms could be interpreted as production/degradation within the L1 layer or influx/efflux from the surroundings. The complete auxin model is described by

$$\frac{dA_i}{dt} = c_A - d_A A_i + c_{A2} X_i + D \sum_{k \in \mathcal{N}_i} (A_k - A_i) + T \sum_{k \in \mathcal{N}_i} (P^*_{ji} \frac{A_j}{K_A + A_j} - P^*_{ij} \frac{A_i}{K_A + A_i}) \quad \text{(S5)}$$

where the summations are over the set of cell neighbors, $\mathcal{N}_i$. X_i is a molecule not present in the central zone (as described below), and the X dependent auxin production is used to break the symmetry and decrease the probability of peak formation in the central zone. Parameter values used in the presented simulations are $D = 0.01$, $T = 0.036$, $K_A = 1.0$, $c_A = 0.0$, $c_{A2} = 0.002$ and $d_A = 0.001$.

PIN1 model

For the PIN1 polarization we use the linear auxin dependance, $f(A_j) = k_1 A_j$ in equation 4 in the paper, and assume equilibrium concentrations leading to

$$P_{ij}^{*} = \frac{k_1 A_j P_i^{tot}}{k_2 + \frac{k_1}{|\mathcal{N}_i|} \sum_{k \in \mathcal{N}_i} A_k} \tag{S6}$$

where P_i^{tot} is the total amount of PIN1 in the cell and is assumed to be constant in these simulations ($P_i^{tot} = 1, \forall i$). We use $k_2/k_1 = 0.3$ and the summation is again over the set of cell neighbors, $\mathcal{N}_i$. The number of neighbors $|\mathcal{N}_i|$ enters as a spatial contribution where membrane sizes are approximated to be equal for all membranes surrounding a cell.

Central zone definition

The central zone peripheral zone difference is defined in the model by using a molecule X that is produced only outside an apical region, and degraded everywhere. This molecule is allowed to diffuse, and it induces auxin production. The ODE describing the dynamics is given by

$$\frac{dX_i}{dt} = c_X \Theta(\sqrt{x_i^2 + y_i^2} - R_X) - d_X X_i + D_X \sum_{k \in \mathcal{N}_i} (X_k - X_i) \tag{S7}$$

where the summation is over the set of cell neighbors, $\mathcal{N}_i$, and the step function $\Theta(x)$ equals 1 for $x \geq 0$ and zero for $x < 0$. In all simulations, parameter values $c_X = 0.1$, $d_x = 0.1$ and $D_X = 0.01$ has been used. Two values of $R_X = \{1.5, 2\}$ are used in the half-sphere cylinder simulations (Figure 5 in the paper), and $R_X = 2.0$ is used in the reversal simulation (Figure 6 in the paper).

Cell growth and proliferation model

Cells are modeled as spheres with a radial growth described by

$$\frac{dr_i}{dt} = k_{growth} r_i \left(1 - \frac{r_i}{r_{max}}\right) \tag{S8}$$

In the half-sphere cylinder simulations (Figure 5 in the paper), parameter values $k_{growth} = 0.002$ and $r_{max} = 2.0$ are used for cells on the half-sphere, while the growth is truncated ($dr_i/dt = 0$) for cells on the cylinder surface ($z < 0$). For the reversal simulations on the two-dimensional plane (Figure 6 in the paper), $k_{growth} = 0.002$ and $r_{max} = 2.0$ is used for all cells. To produce the plots, the simulation is stopped when a peak is about to form, and then restarted with zero growth rate ($k_{growth} = 0.0$). The reason for this is that it easier to follow the polarization reversal if there are no dividing cells in the neighborhood.

Cells divide when they are larger than a threshold value ($r_i > 0.9$). At division, two new cells conserving the mass of the mother cell are created with a random deviation

of the individual sizes of $V_1 = (0.5 \pm k_{diff})V$, $V_2 = (0.5 \mp k_{diff})V$, where V is the size of the mother cell and V_1, V_2 are the sizes of the daughter cells and $k_{diff} = 0.2$ is used. Initially at division the two new cells are placed at a random direction on the surface, a distance $h = 0.3r_{mother}$ apart, centered around the mother position. The molecular concentrations in the daughter cells are inherited from the mother.

In the half-sphere cylinder simulations, cell division is only present at the apex ($R_{xy} < 5.0$), while there is no cell division further down. Together with the growth truncation (at $R_{xy} >= 7.0$), this leads to a shoot that has an apical region with cellular growth and division, one region where growth but not division is present, and lastly, a region without growth or divisions.

Mechanical interactions

Mechanical interactions are modeled using overdamped spring forces (two-dimensional versions of $dx_i/dt = k_{spring}((x_j - x_i) - d_{relax})$, where x_i, x_j are the positions of cells i, j and d_{relax} is the resting length of the spring) between neighboring cells [9, 3, 4]. In the presented simulations, we have only used a repulsive interaction when the distance between the cell centers is less than the resting length of the spring. The resting lengths of the springs allow for an overlap of the spheres ($d_0 = f_{ov}(r_1 + r_2)$), where r_1, r_2 are the radii of the cells.) In the simulations, parameter values $k_{spring}^{repulsive} = 0.2$, ($k_{spring}^{adhesive} = 0.0$), and $f_{ov} = 0.75$ are used.

The calculations of the spring forces in a two-dimensional plane, as used in the reversal simulation, are straightforward. When the cells are restricted to the half-spherical surface, the curvature needs to be included. Distances are measured using the shortest distance (following the great circle passing through the cell centers). When calculating the total positional update for a cell, forces from all neighbors are added up on the tangential plane to the half-sphere surface defined at the current cell position. After the movement in this plane, the cells are projected down to the half-cylinder surface.

Neighborhood

Neighbors for cells are defined at each time step as cells (spheres) that have an overlap, $d_{12} < r_1 + r_2$, where d_{12} is the distance between the cell centers, and redefined directly at division for the dividing cells. This is determining which cells that have transport in-between each other as well as which cells that (potentially) interact mechanically.

S3 Possible mechanism for auxin feedback to PIN1 cycling

All of the differential equation terms in Table S1 and S3 follow from the corresponding reaction mechanisms under either the law of mass action or the M-M approximation in enzyme kinetics, with the exception of the reaction governing auxin feedback from cell j to PIN1 cycling in cell i with Hill function or linear rate law. We now exhibit an example

mechanistic model which can relate this reaction and the differential equation term we have used for it.

The mechanistic model is in the form of a feedback pathway from auxin in cell j, to the PIN1 cycling in cell i from the central cytosolic compartment i to the boundary compartment (ij) with cell j. All reactions in this pathway are assumed to be fast with respect to those of Table S1, except for the final feedback regulation of the transport $P_i \rightarrow P_{ij}$. The pathway contains four new protein players (Table S4): two proteins Y_j and B_{jn} that amplify auxin in cell j by a Hill's function; a ligand L_{ji} that carries this signal to the boundary of cell j with cell i; a receptor R_{ij} in cell i that receives the signal by binding with L_{ji} (forming a receptor- ligand complex denoted C_{ij}); and a second messenger M_{ij} that is activated by C_{ij} to form M^*_{ij}, the catalyst for the transport reaction $P_i \rightarrow P_{ij}$. All these reactions are shown in Table S5, broken down into subnetworks 1, 2, and 3. These reactions and subnets are also shown in machine-executable form in the Cellerator [10] notebook feedbackpath.nb. The exact rate law for reactions 1 and 2 follow from the concept that there are n identical and non-interacting auxin-binding sites on protein B. If $m-1$ of them have auxin already bound, then binding reactions $B_{j(m-1)} \rightarrow B_{jm}$ proceed in proportion to the number of unbound sites $(n-(m-1))$. If m sites are occupied, then unbinding reactions $(B_{jm} \rightarrow B_{jm-1})$ proceed in proportion to m. This explains the constants in the reaction schema proposed.

The assumptions of low occupancy for reactions 1 and 2, and high occupancy of reaction

7, in Table S5 are satisfied if we have the limits

$$\frac{k'_f}{k'_r}A_j << 1, \text{, and} \tag{S9}$$

$$K'_M << M_{ij}^{tot}, \tag{S10}$$

where $M^{tot} = M_{ij} + M_{ij}^*$ is constant. Under these assumptions, it is possible to derive the equilibrium conditions for each subnetwork above. They are:

Subnet1: $B_{jn} = B_T k'^n_f A_j^n / k'^n_r$, where $B_T = \sum_l B_{jl}$. This raises auxin to the n'th power.

Subnet 2: $L_{ji} = (v'/k')Y_j A_j^n/(K_{Hill}^n + A_j^n)$, where $K_{Hill} = (K'/B^T)^{1/n} k'_r/k'_f$. This provides a Hill's function.

Subnet 3: $M_{ij}^* = V_{eff} A_j^n/(K_{Hill,eff}^n + A_j^n)$, where $K_{Hill,eff} = (k'k'_4 K_{Hill}^n/(k'k'_4 + k'_3 v' Y_j))^{1/n}$, and $V_{eff} = k'_3 v' v'_1 R_{ij}^T Y_j/(k'_2(k'k'_4 + k'_3 v' Y_j))$, where $R_{ij}^T = R_{ij} + C_{ij}$. This moves information in the form of a Hill's function from cell j to cell i.

Finally subnet 4 moves slowly, with rate in direct proportion to the catalyst M^* which is present proportionate to the Hill's function of auxin in cell j:

$$M_{ij}^* = \frac{V_{eff} A_j^n}{K_{eff}^n + A_j^n} \tag{S11}$$

The final rate law is then

$$\frac{dP_{ij}}{dt} = k'_1 M_{ij}^* P_i - k_2 P_{ij} \tag{S12}$$

Table S4: Example feedback pathway players

Row	Molecule	Description
1	A_j	auxin in (neighboring) cell j (as already in paper)
2	$B_{j(m)}$	n-sited auxin-binding protein, with any m out of n sites filled
3	Y_j	a one-sited enzyme that converts B into ligand L
4	L_{ji}	ligand in cell j, adjacent to cell i
5	R_{ij}	receptor in cell i, adjacent to cell j
6	C_{ij}	activated receptor-ligand complex in cell i, adjacent to cell j
7	M_{ij}	second messenger in cell i, adjacent to cell j
8	M^*_{ij}	activated second messenger in cell i, adjacent to cell j
9	P_i	cytosolic PIN1 in cell i (as already in paper)
10	P_{ij}	PIN1 in cell i, adjacent to cell j (as already in paper)

as claimed. Note that the Hill function becomes linear, so that $f(A) = A$, in the limit $n = 1$, $K_{eff} >> A_j$.

Thus, the rate law in reaction 9 of Table S1 has at least one possible mechanistic realization in the form of a feedback pathway that includes a new receptor, ligand, and second messenger. Many other detailed hypotheses are also possible and would do the same job.

S4 PIN1 cycling parameter optimization

To be able to optimize the PIN1 cycling model using the two-dimensional single-time point template of PIN1 some assumptions are necessary. (1) The molecular transport and reactions involved are fast compared to the growth of the plant such that the concentrations within compartments can be assumed to be in or close to equilibrium. (2) The detailed auxin transport model provides a good estimation of the auxin equilibrium

Table S5: Example feedback pathway reactions

Row	Reaction	Rate
Subnet 1 (fast): $(m \in \{1, ..n\})$		
1	$B_{j(m-1)} \overset{A_j}{\rightarrow} B_{j(m)}$	$A_j(n-m+1)k'_f B_{j(m-1)}$
2	$B_{j(m)} \rightarrow B_{j(m-1)}$	$B_{j(m)} m k'_r$
Subnet 2 (fast):		
3	$B_{j(n)} \overset{Y_j}{\rightarrow} L_{ji}$	$\frac{v' Y_j B_{jn}}{K' + B_{jn}}$
4	$L_{ji} \rightarrow B_{j(n)}$	k'
Subnet 3 (fast):		
5	$L_{ji} + R_{ij} \rightarrow C_{ij}$	$k'_3 L_{ji} R_{ij}$
6	$C_{ij} \rightarrow L_{ji} + R_{ij}$	$k'_4 C_{ij}$
7	$M_{ij} \overset{C_{ij}}{\rightarrow} M^*_{ij}$	$\frac{v'_1 C_{ij} M_{ij}}{K'_1 + Mij}$
8	$M^*_{ij} \rightarrow M_{ij}$	$k'_2 M^*_{ij}$
Subnet 4 (slow):		
9	$P_i \overset{M^*_{ij}}{\rightarrow} P_{ij}$	$k'_1 M^*_{ij}$
10	$P_{ij} \rightarrow P_i$	k_2

concentrations given PIN1 localization as input. Given these assumptions, we use the following schema to optimize the PIN1 cycling models:

1. We simulate the detailed auxin transport model until equilibrium is reached using static compartmental topologies and PIN1 concentrations as extracted from the template (Figure 1D in the paper).

2. We simulate the PIN1 cycling model until equilibrium is reached (or calculate equilibrium concentrations) using static compartmental topologies, cellular PIN1 contents as extracted from the template, and static auxin concentrations resulting from the previous step. Cellular PIN1 contents are the total amount of PIN1 in the cellular compartment and connected membranes (Figure 1C in the paper).

3. We use an objective function to determine the difference of PIN1 localization between template and model. We use an average squared error as objective function $E = 1/N_{comp} \sum^{N_{comp}} (P_{comp}^{template} - P_{comp}^{model})^2$, where N_{comp} is the number of compartments, and $P_{comp}^{template}$,P_{comp}^{model} are the PIN1 concentrations from the template and model respectively.

4. We redo step 2 and 3 using an optimization algorithm by which parameters are adjusted until optimal values are found.

For step 2 in the optimization procedure, we use the analytically calculated equilibrium concentrations for the comparison to the extracted template values. The PIN1 equilibrium (from Equations S3,S4) and $P_i^{tot}V_i^{tot} = P_iV_i + \sum_{k\in\mathcal{N}_i} P_{ik}a_{ik}$) are given by

$$P_i^* = \frac{K_P P_i^{tot} V_i^{tot}}{K_P V_i + \sum_{k\in\mathcal{N}_i} \frac{A_k^n}{K^n + A_k^n} a_{ik}}, \tag{S13}$$

$$P_{ij}^* = \frac{\frac{A_j^n}{K^n + A_j^n} P_i^{tot} V_i^{tot}}{K_P V_i + \sum_{k\in\mathcal{N}_i} \frac{A_k^n}{K^n + A_k^n} a_{ik}}, \tag{S14}$$

where $P_i^{tot}V_i^{tot}$ for different cells are measured in the experimental template. Since the equilibrium concentrations are used in the optimization, only the relative strengths of the cycling rates ($K_P = k_2/k_1$) can be optimized, together with the Hill coefficient, and constant, n, K. We use a simple local search algorithm, where a single parameter is randomly chosen and multiplied (or divided) by a factor 1.01. The algorithm is greedy and the new parameter value is only kept if the cost E is lowered. Using multiple

restarts with random initial parameter values suffice to find good solutions. There is a well defined region in parameter space that corresponds to good solutions as can be seen in Figure S6A, and solutions found when the local optimizer is restarted 100 times is shown in Figure S6B.

S5 Analysis of the simplistic model

To further investigate the behavior of the simplified model, we have carried out a linear stability analysis of Equation 4 in the paper at the homogeneous fixed point ($A_i = A, \forall i$) in the one-dimensional periodic case. The Jacobian matrix, $J_{ij} = df_i/dA_j$ has elements defined by

$$J_{ij} = 0, |i-j| > 2, \tag{S15}$$

$$J_{ij} = -\frac{TP}{4}, |i-j| = 2, \tag{S16}$$

$$J_{ij} = D + \frac{TP}{2}, |i-j| = 1, \tag{S17}$$

$$J_{ij} = -2D - \frac{TP}{2}, |i-j| = 0, \tag{S18}$$

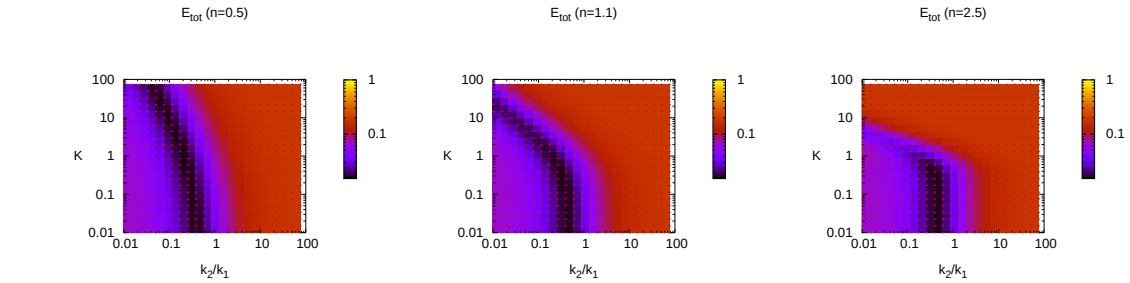

A.

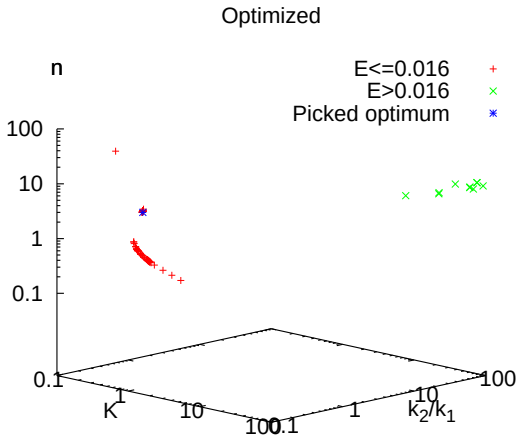

B.

Figure S6: Optimization for the PIN1 cycling model using a non-linear auxin dependence for the cellular to membrane term. The parameters that are optimized and shown in the plots are the relative internalization/membranalization strengths, $K_P = k_2/k_1$, and the Hill coefficient and constant, n, K. A) Mean squared error, E_{tot} for different parameter values. B) Solutions found by restarting the local optimizer 100 times with different initial parameter values. The optimimum parameter set chosen for further investigations is also marked in the plot ($n = 3.0$, $K = 0.4$, and $K_p = 0.4$).

and the eigenvalues of this matrix determine the stability of the homogeneous state [11]. The matrix is translationally invariant, and the eigenvalues are given by

$$\lambda_p = \sum_k J_{k0} e^{-ipk} \tag{S19}$$

$$= -(2D + \frac{TP}{2})e^0 + (D + \frac{TP}{2})(e^{-ip} + e^{-ip}) - \frac{TP}{4}(e^{-2ip} + e^{-2ip}) \tag{S20}$$

$$= -2D + (2D + TP)\cos(p) - TP\cos^2(p), \tag{S21}$$

where $p = 2\pi p_k/N$, and N is the number of cells, and $p_k \in [0..N-1]$ ($p \in [0:1)$). The eigenvalues for different parameter values are shown in Figure S7A for continuous values of p (infinite sized lattice). As can be seen in the figure, some parameter values give rise to positive eigenvalues, leading to instability of the homogeneous fixed point. The constraint on the parameters for an unstable homogeneous state can be defined by looking at the largest eigenvalue ($\lambda_{max} > 0$) among the allowed p values and leads to $D/TP < 0.5$. The conclusion is that for large enough active transport, the homogeneous fixed point is unstable and a small deviation from this will result in spatially patterned auxin concentrations.

To conclude the analysis presented here, we have also looked at the eigenvectors connected to the maximal eigenvalues. The eigenvectors can be written as $A_k = exp(\pm ipk)$, and since p for the maximal eigenvalues larger than zero is restricted to $p \in [0, \pi/3]$ the wavelength of the eigenvectors, ω_k, in cell space are restricted by $6 \leq \omega_k \leq \infty$ (Figure S7B). Hence the patterns are in an initial phase when leaving the unstable homogeneous

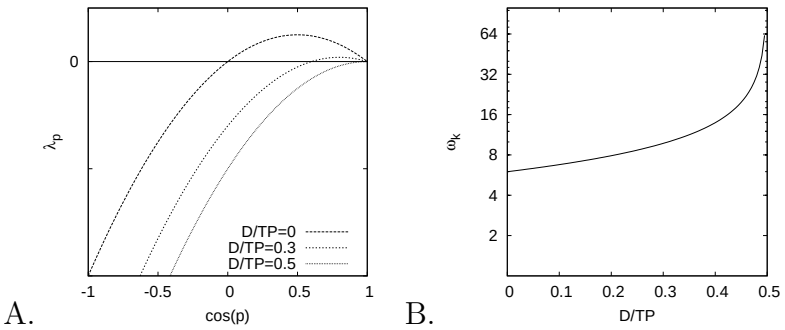

Figure S7: A) Eigenvalue distribution for similar values of D/TP as used in the simulations presented in Figure 3 in the paper. The homogeneous state is unstable if the maximal eigenvalue is larger than zero. B) Distance between peaks at initial dynamics around the unstable homogeneous fixed point as a function of D/TP.

fixed point peaks at least six cells apart, and, in theory, there is no upper limit on the distance between peaks in this infinite one-dimensional case. The analysis is an investigation of the behavior close to the homogeneous state where not only the maximal eigenvalue is positive. The dynamics away from this state are not analyzed using this linear approach, but the final equilibrated states (Figure 3 in the paper) still show nice resemblance of the initial breaking patterns from the analysis. It should be noted that while we have presented this analysis for a simplistic description of the model to clarify the underlying dynamics, analysis of models using a more detailed description of cycling and transport leads to similar conclusions, including analysis of models including cellular and wall compartments explicitly.

S6 Tools and implementation details

S6.1 Image processing tools

The image analysis tools are described in some detail in [5]. The background extraction, uses a matlab script which utilizes the GVF-package [12] (http://iacl.ece.jhu.edu/projects/gvf/). We are greatful to Ylva Aspenberg for the implementation. The other image processing tools used are special purpose software written in C++. The software is built around a watershed [2] type of algorithm and is applicable to two and three dimensional (confocal) images.

S6.2 Modeling tools

All models are simulated in a C++ program which numerically solves the ODE equations using a 5th order Runge-Kutta solver with adaptive time steps [8]. It allows for changes in the number of variables and equations (e.g. at cell divisions) during the simulations. It includes an extendable library of reaction, transport, growth, and mechanical interaction mechanisms suitable for developmental and multicellular simulations.

S6.3 Visualization tools

Model results are visualized using C++ programs that reads the simulator output and creates tiff (Figures 1, 2, 4, 5) or postscript (Figure 6) output. The three-dimensional visualizations (Figure 5 and Supplementary movies) use openGL (http://www.opengl.org) and produces tiff files as output. Movies from these tiff files are created using Quicktime Professional (http://www.apple.com). Plots (Figures 3,4) are created using gnuplot (http://www.gnuplot.info).

References

[1] Goldsmith, M.H., Goldsmith, T.H., Martin, M.H. (1981) Mathematical analysis of the chemosmotic polar diffusion of auxin through plant tissues, *Proc Natl Acad Sci U S A.*, **78**(2), 976-980.

[2] Gonzalez, R.C., R.E. Woods (2002) Digital image processing, Addison-Wesley, Reading, MA.

[3] Jönsson, H., B.E. Shapiro, E.M. Meyerowitz, E. Mjolsness (2004) Modeling plant development with gene regulation networks including signaling and cell division, in Kolchanov, N., R. Hofestaedt (eds.), Bioinformatics of genome regulation and structure, Kluwer Academic Publishers, Boston.

[4] Jönsson, H., A. Levchenko (2005) An explicit spatial model of yeast microcolony growth, *Multiscale Modeling and Simulation*, **3**, 346-361.

[5] Jönsson, H., Heisler, M., Reddy, V.G., Agraval, V., Gor, V., Shapiro, B.E., Mjolsness, E., Meyerowitz, E.M. (2005) Modeling the organization of the WUSCHEL expression domain in plants, *Bioinfomatics* **21**, i232-i240.

[6] Kramer, E.M. (2004) PIN and AUX/LAX proteins: their role in auxin accumulation, *Tr. Plant Sci.* **9**(12), 578-582.

[7] Mitchison, G.J. (1980) The dynamics of auxin transport *Proc. R. Soc. Lond.* **B209**, 489-511.

[8] Press, W.H., S.A. Teukolsky, W.T. Vetterling, B.P. Flannery (1992) Numerical recipes in C The art of scientific computing, Cambridge University Press, New York.

[9] Shapiro, B.E., E. Mjolsness (2001) In *Proceedings of the second international conference on systems biology*, pp 342-351.

[10] Shapiro, B.E., Levchenko, A., Meyerowitz, E.M., Wold, B.J., Mjolsness, E.M. (2003) Cellerator: extending a computer algebra system to include biochemical arrows for signal transduction simulations, *Bioinformatics* **19**, 677-678.

[11] Strogatz, S. H. (1994) Nonlinear dynamics and chaos, Perseus Books Publishing, Cambridge, MA.

[12] Xu, C., J. L. Prince (1998) Snakes, shapes, and gradient vector flow, *IEEE Transactions on Image Processing*, **7**, 359-369.